



# Resistance spot welding of dissimilar material joints with a cold-gas-sprayed inlayer

Christian Hagen<sup>1</sup> · Franz-Josef Klinkenberg<sup>1</sup> · Ralf Ossenbrink<sup>2</sup> · Vesselin Michailov<sup>2</sup>

Received: 19 April 2023 / Accepted: 30 June 2023 / Published online: 20 July 2023  
© The Author(s) 2023

## Abstract

In this publication, cold gas spraying (CGS) is investigated as an enabler for aluminum-steel joints. Using a powder-based coating process to adhere a steel layer to an aluminum substrate allows a steel component to be welded to the deposited layer by resistance spot welding. This method permits the metallurgical connection between similar materials to be separated, while mechanical bonding ensures the connection at the dissimilar aluminum-to-inlayer interface. A modification of the porous CGS layer, as well as the creation of the remelted zone in the aluminum, can be observed during the resistance spot welding process. Electron backscatter diffraction (EBSD) analyses show that the severely prestressed particles in the CGS coating recrystallize, which coincides with a decrease in defect density and hardness in the heat-affected zone. Microscopy of the aluminum substrate shows the creation of metallurgical pores as well as the expansion of pores attributed to the casting process. The rise in remelted aluminum hardness and decrease in the heat-affected zone of the CGS layer indicate the formation of a metallurgical notch.

**Keywords** Resistance spot weld · RSW · Cold gas spray · CGS · Inlayer · Dissimilar joint · Aluminum-steel weld

---

**Highlights** Aluminum to steel weld by application of a cold-gas-sprayed inlayer.

Welding dissimilar materials with identical equipment as similar materials.

Recrystallization of the cold-gas-sprayed inlayer near the welding nugget.

Micro-alloyed steel to high-pressure die cast aluminum joining.

---

✉ Christian Hagen  
christian.ha.hagen@bmw.de

Franz-Josef Klinkenberg  
franz-josef.klinkenberg@bmw.de

Ralf Ossenbrink  
ralf.ossenbrink@b-tu.de

Vesselin Michailov  
michailov@b-tu.de

<sup>1</sup> BMW AG, Ohmstraße 2, 84034 Landshut, Germany

<sup>2</sup> Lehrstuhl Füge- und Schweißtechnik Brandenburgische, Technische Universität Cottbus-Senftenberg, Konrad-Wachsmann-Allee 17, 03046 Cottbus, Germany

## 1 Introduction

To meet the evolving requirements of lightweight structures in the transport sector, such as increased driving range and higher crash resistance, a so-called multi-material lightweight design is applied. This design principle is based on the use of specific materials to meet the requirements of the component. This implies the necessity of joining aluminum alloy and high-strength steel. Currently, in the automotive industry, aluminum-to-steel connections are widely executed by self-piercing rivets, for which sufficient dynamic elongation of the materials must be ensured [1]. With the current shift from internal combustion engines to electric driving, there is a renewed emphasis on the utilization of massive aluminum die cast components to minimize vehicle complexity and allow for lighter automobile constructions. To ensure dimensional accuracy of the casted components, subsequent heat treatment is dispensed with, which leads to a reduction in available ductility [2]. This results in cracking of the high-pressure die cast component, which impairs the mechanical properties, resulting in the need for novel joining techniques.

Conventional fusion welding methods such as resistance spot welding, laser welding, and arc welding have

been studied continuously for the joining of aluminum to steel. Welding these dissimilar materials poses challenges due to the formation of intermetallic phases (IMP) [3, 4]. A metallurgical connection is created by the brittle IMP between the joint partners. The brittleness of these phases has an unfavorable impact on the connection's ductility and fatigue strength with thicker layer thicknesses. To reduce the development of IMP, additional materials can be used which results in better mechanical properties. In the resistance spot welding process, which is widely used in the automotive industry, these additional materials can be applied by coating [5, 6] or transition tape [7] between the joint partners.

Through the application of a cold-gas-sprayed (CGS) intermediate layer, the separation of the aluminum-to-layer and layer-to-steel connections can be achieved, the former by mechanical clamping and the latter by metallurgical bonding. As a result, load transition does not employ intermetallic phases. CGS is an all-solid-state, high-kinetic-energy coating process in which micron-sized solid particles are accelerated with high-pressure compressed gas onto a substrate in atmospheric conditions [8]. By exceeding a critical velocity, the particles carry enough energy to adhere to the substrate, where they deform intensely, resulting in a deposition of particles on the substrate and forming a porous layer [9, 10]. Depending on the particle velocity, the deformation and therefore the residual stress in the particle correspond with the compactness of the layer [9, 11]. The technology of CGS is currently used in wear minimization and functionalization of surfaces [12, 14].

In this publication, an inlayer applied by cold gas spraying is investigated as an intermediate layer for resistance spot welding in mixed material joints as an alternative to mechanical joining techniques for steel and aluminum. In previous studies, the use of a CGS layer for aluminum-steel dissimilar joints with the use of a resistance spot welding process was explored with a layer consisting of aluminum, nickel, or a mixture of both applied to steel and later welded or brazed to aluminum [4, 15]. In contrast, a steel inlayer is attached to the aluminum substrate and then welded to a steel joint partner in this experiment enabling the use of welding equipment made for steel welds. During the welding

process, the formation of the welding nugget results in a modification of the surrounding materials. The cold-gas-sprayed layer will recrystallize in the heat-affected zone, and the aluminum will form a remelted zone near the nugget. This reduction in hardness of the formerly work-hardened layer indicates the formation of a metallurgical notch. The formation of pores at the aluminum-to-CGS interface shows the combination of trapped gases from the casting process and metallurgical pores formed during weld solidification in remelted aluminum.

## 2 Material and experimental procedures

In this investigation, a 316L stainless steel powder is used to process the intermediate layer on the AlSi10MnMg aluminum die cast substrate, which is later welded to a 1.0991 steel plate. The chemical compositions of the aluminum material were obtained by optical emission spectrometer (OES) analysis, which was conducted with a model ARL 4460 from Thermo Scientific, USA. The 316L powder and steel plate were analyzed by inductively coupled plasma (ICP) OES, aided by a carbon/sulfur (C/S) detector to determine the carbon and sulfur content. The equipment used for analyzing the chemical composition of the iron-based materials was the ICP-OES analyzer type 720-ES by Agilent Technologies, Inc., USA, and the C/S detector type CS744 by Leco Instrumente GmbH, Germany. The results of the chemical compositions are summarized in Table 1.

The near-eutectic aluminum alloy AlSi10MnMg is a common material used for large high-pressure die cast structures in the automotive sector due to its good casting and mechanical properties. In its non-heat-treated state, as used in this study, the offset yield strength  $R_{p0.2}$  is 130MPa with an elongation at break of 4% for 3-mm-thick casted material. In its as-casted state, the hardness in the microsection depends on the distance to the surface of the component. Due to the rapid cooling near the aluminum-to-die interface and a reduced cooling rate near the core, the hardness near the edge is with 95HV which is higher than that of the

**Table 1** Chemical composition of the materials in this study in wt.%

Aluminum high-pressure die casting alloy AlSi10MnMg (measured by OES)									
Si	Fe	Cu	Mn	Mg	Zn	Ti	Sr	Al	
10.45	0.13	0.033	0.57	0.39	0.008	0.07	0.02	Balance	
Austenitic stainless steel 316L (measured by ICP-OES and C/S)									
Cr	Ni	Mo	Mn	Si	P	C	S	Fe	
16.6	10.4	2.17	1.62	0.87	0.020	0.02	0.004	Balance	
Micro-alloyed steel 1.0991 (measured by ICP-OES and C/S)									
C	Si	Mn	P	S	Al	Ti	Nb	Cu	Fe
0.07	0.4	1.0	0.020	0.004	0.04	0.03	0.05	0.008	Balance

measurements at the core, which reach 70HV. The material was provided by BMW AG, Germany.

The 316L powder was sourced from Sandvik AB, Sweden, in powder grain sizes between 15 and 38 $\mu\text{m}$  and processed with the CGS equipment of Impact Innovations GmbH, Germany. For applying the CGS layer to the aluminum, a 5/11 EvoCSII CGS-Gun in combination with an 8-mm Laval nozzle is used. With 1100°C and 50bar, the nitrogen gas accelerates the particles to a velocity of 630 to 780m/s depending on the particle size. Through the deformation of particles and substrate, a steel layer can be deposited on the aluminum substrate. The resulting cold-gas-sprayed layer is fully austenitic and porous [13, 16]. Due to the high deformation, a hardness of around 390HV is reached in this configuration. The absolute hardness values between other investigations cannot be compared due to different coating parameters [12, 13] and particle sizes [10] and therefore varying deformation rates. The coating is displayed as an overview in Fig. 1a and in detail in Fig. 1b. In this detailed microsection, the lamellar structure can be observed by etching it with 3% HNO<sub>3</sub>. The compacted layer shows deformed particles, which are boarded by particle-to-particle interfaces, displayed in black lines. At the interfaces, defects occur due to insufficient deformation of the deposited and newly applied particles. The defects in the displayed section are highlighted in red. The majority of defects are in the range of 10 to 100  $\mu\text{m}^2$ , although there are individual accumulations of defects that can reach up to 600  $\mu\text{m}^2$ . The last layer of particles will not be deformed in a lamellar structure by following particles, resulting in a rough surface with an  $R_z$  of 59 $\mu\text{m}$ .

The 316L powder was sourced from Sandvik AB, Sweden, in powder grain sizes between 15 and 38 $\mu\text{m}$  and processed with the CGS equipment of Impact Innovations GmbH, Germany. For applying the CGS layer to the aluminum, a 5/11 EvoCSII CGS-Gun in combination with an 8-mm Laval nozzle is used. With 1100°C and 50bar, the nitrogen gas accelerates the particles to a velocity of 630 to 780m/s depending on the particle size. Through the deformation of particles and substrate, a steel layer can be deposited on the aluminum substrate. The resulting

cold-gas-sprayed layer is fully austenitic and porous [13, 16]. Due to the high deformation, a hardness of around 390HV is reached in this configuration. The absolute hardness values between other investigations cannot be compared due to different coating parameters [12, 13] and particle sizes [10] and therefore varying deformation rates. The coating is displayed as an overview in Fig. 1a and in detail in Fig. 1b. In this detailed microsection, the lamellar structure can be observed by etching it with 3% HNO<sub>3</sub>. The compacted layer shows deformed particles, which are boarded by particle-to-particle interfaces, displayed in black lines. At the interfaces, defects occur due to insufficient deformation of the deposited and newly applied particles. The defects in the displayed section are highlighted in red. The majority of defects are in the range of 10 to 100  $\mu\text{m}^2$ , although there are individual accumulations of defects that can reach up to 600  $\mu\text{m}^2$ . The last layer of particles will not be deformed in a lamellar structure by following particles, resulting in a rough surface with an  $R_z$  of 59 $\mu\text{m}$ .

The joint partner used in this study is 1.0991 with a thickness of 1.6 mm, which is a micro-alloyed steel plate used in automotive production for middle to highly stressed components. In its thermally unstressed state, the micro-alloyed steel reaches a hardness of 195 HV. The ferritic steel is zinc-plated by hot-dip galvanizing with 50 g/m<sup>2</sup>. The resistance spot welding process was carried out using a servo-pneumatic welding gun produced by BMW AG, Germany, equipped with a medium-frequency direct current welding electronic by Bosch Rexroth AG, Germany. The maximum electrode force is 5.5kN and the maximum allowed electrical current is 14.5 kA. In this study, CuCrZr-electrodes of type B with a tip diameter of 7 mm are used on both sides of the joint.

Microsections, hardness maps, scanning electron microscope (SEM) analysis, and electron backscatter diffraction (EBSD) analysis are used to describe and evaluate the weld joint. The equipment used for this analysis was a Zeiss EVO 60 XVP and an Oxford Symmetry. The microhardness measurements were conducted with the help of a Qness Q10A + hardness tester.

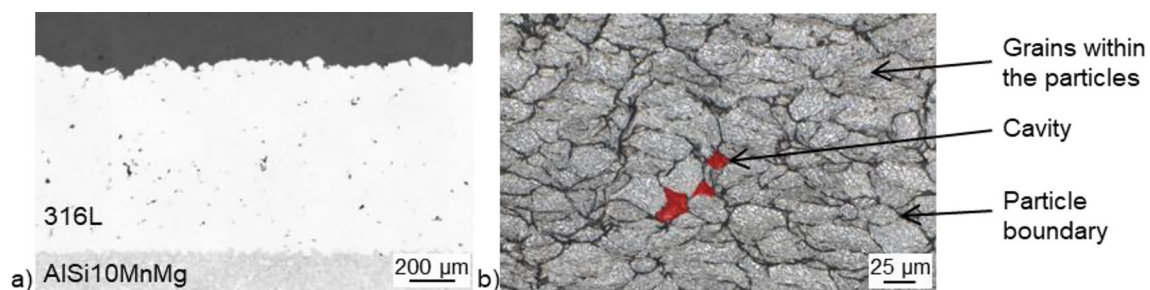


**Fig. 1** Cold-gas-sprayed inlayer in an as-sprayed state. **a** Overview and **b** detail of the 316L inlayer; the cavities are highlighted in red

The term “pores” will be used to describe the pores that occur during the welding process, whereas “defect” will be used to describe the porosity of the sprayed layer caused by the coating process.

### 3 Results

#### 3.1 Welding process

The resistance spot welding process of an interlocked, porous, and work-hardened interlayer results in a characteristic phenomenon in the process monitoring which is presented in this subsection, as well as the influence of the

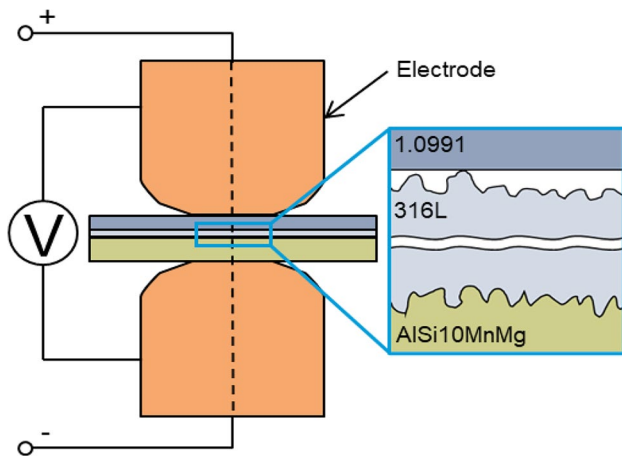


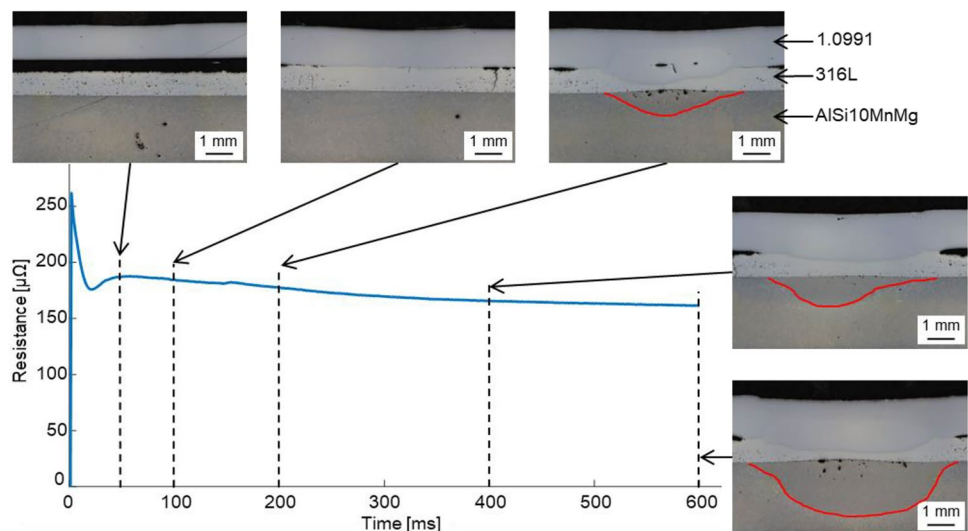
**Fig. 2** Schematic of the resistance spot welding with a cold-gas-sprayed inlayer with a detail of the contact areas between the joint partners as well as the schematic circuit diagram for resistance measurement

formation of the welding nugget on the lower melting aluminum substrate.

In the configuration displayed in Fig. 2, two separate and vastly different contact areas between the materials can be observed. The mechanical clamping of the particles in the aluminum results in a large contact area between the aluminum and the CGS layer, while the partly deformed particles form a rough surface, which subsequently leads to a reduced contact area with the steel plate. The contact area between the aluminum-to-CGS is therefore considerably larger than that of CGS-to-steel faying surface in the same projected area. This leads to a higher resistance at the faying surface, reducing the influence of the electric resistance at the aluminum-to-CGS interface.

During the welding process, the profile of the dynamic resistance is recorded by measuring the total resistance of the joint, as pictured diagram in Fig. 2. Based on the resistance curve, the formation of a weld can be observed in the process monitoring software. The resistance curve in Fig. 3 represents the average of three welds with a constant current of 9 kA and an electrode force of 5 kN. The microsections exhibited were created on specimens where the welding duration was terminated at the time specified. The maximal evaluated welding time is 600 ms. A peak in the dynamic resistance curve due to the high contact resistance between the aluminum and the electrode before rupturing the oxide layer is perceptible. Subsequently, the formation of a plateau similar to steel-to-steel welds can be observed by the characteristic rise of the dynamic resistance due to the increase in the material resistance of the steel partners. The specimen welded with 50ms does not form a bond, resulting in a separation of the joint partners in the microsection. At this weld time, only the zinc coating of the steel plate experiences a modification in the faying surface by melting. Neither the formation of a weld nor a change in the microstructure of the

**Fig. 3** Resistance curve of a resistance spot weld with CGS inlayer and microsections at different time steps





cold-gas-sprayed layer can be noted. At 100 ms, a reduction of the defect density in the cold-gas-sprayed layer, compared to the microsection at 50 ms, can be noted as the first modification of the materials in the weld. The nugget starts to form in the faying surface between 100 and 200 ms accompanied by a further reduction of defect density in the cold-gas-sprayed inlayer. After 200 ms, a growth of the nugget can be observed. The growth of the nugget is displayed by a continuous decrease in dynamic resistance [17].

In the microsections starting at 200 ms, the formation of a remelted area in the aluminum can be observed, whose border is marked by a red line. This indicates that the liquid aluminum can infiltrate the porous inlayer. The liquid aluminum contacting the porous inlayer can infiltrate the defects in the coating if they are connected by a path. These paths form along particle boundaries of the coating as the result of improper particle-to-particle bonding. In preliminary tests, a defect rate of 1% was defined as an upper limit to reduce the probability of the aluminum infiltration. The infiltrated aluminum can lead to the mixing of the aluminum and iron, and thus to the formation of intermetallic phases in the nugget, resulting in poor mechanical performance of the spot weld. The defect rate can be influenced by modifying the coating parameters with a higher particle velocity leading to lower defect rates [18].

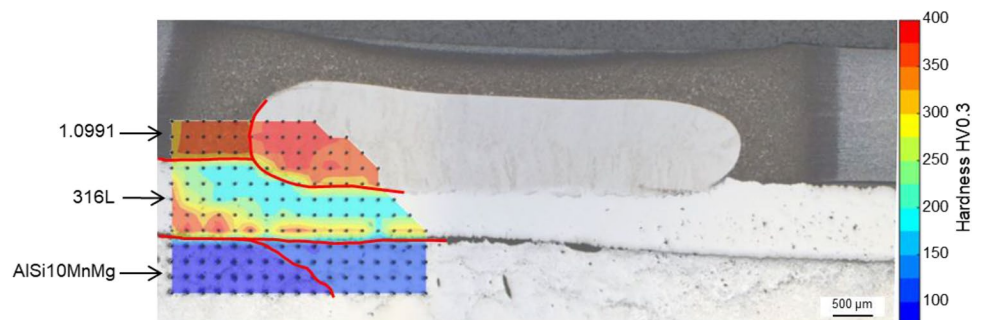
### 3.2 Microstructure of the joint

The microstructure and hardness of the joint and surrounding areas are investigated using light microscopy, SEM, and a hardness tester. An overview of the weld between the CGS layer and the steel plate is displayed in Fig. 4 with an overlaid hardness map. The microsection presented is etched which results in a higher contrast between the heat-affected zone (HAZ) in the micro-alloyed steel and the weld nugget as well as corrosive damage of the aluminum substrate. Overlaid are linear interpolated Vickers hardness measurements for which the nodes were recorded in a  $0.2 \times 0.2$ -mm grid and with an automatic optical microscope that evaluates the diagonals of the indentations generated with a force of 2.942 N. The red lines in the interpolated area mark the

borders between the steel plate, CGS layer, and the aluminum, which is further divided into the as-casted state and the remelted area under the nugget.

In the microsection, a distinct difference between the ferritic steel plate and the austenitic CGS layer can be noted, with the HAZ in the micro-alloyed steel displayed by a darker shade. In the CGS layer, no distinctive HAZ can be observed; only a reduction of defect density near the nugget is detectable. Analogous to the annealing effects in sintering, a reduction of defects due to the progressive metallurgical bonding between the particles during the annealing process, in combination with the electrode forces in the welding process, occurs [19]. The defects on the interparticle boundaries transform into globular micropores on the grain boundaries [20]. The nugget between the CGS layer and steel is composed of a mixture of the micro-alloyed 1.0991 steel plate and the austenitic 316L in the intermediate layer. An unsymmetrical formation between the two steel partners is notable. The proportion by area is about 70/30% with the ferritic steel taking the predominant part. In investigations into the welding of ferritic to austenitic steel, an asymmetrical formation of the weld nugget can be observed due to the different melting temperatures and heat transfer coefficients of the materials [21, 22]. The heat transfer is further reduced by the defects and improper particle-to-particle bonding in the austenitic CGS layer. Contrary to the observations in Fig. 4, where an unsymmetrical formation in favor of the micro-alloyed steel is noticeable, the forementioned literature depicts a formation of the nugget mainly in the austenitic steel. This effect can be explained by the thin layer in combination with the aluminum substrate, which results in a higher thermal conductivity and thus reduces nugget formation on the austenitic side. The microstructure of the weld nugget has martensitic structures, as shown in Fig. 5. Because of the quick cooling process, the supersaturated solution traps carbon in the crystal structure, causing a distortion during the lattice transition during the solidification process, resulting in a fine dislocation substructure. The presence of these structures validates the assumption based on the chemical composition of the nugget,

**Fig. 4** Microhardness mapping overlaying the region of the spot weld in an etched microsection



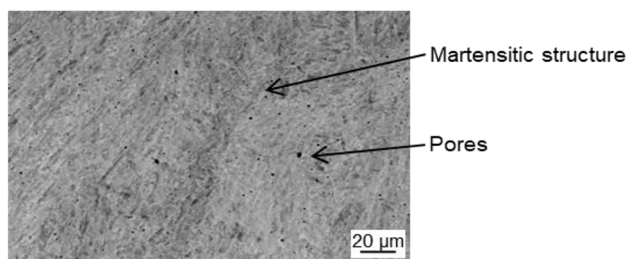


**Fig. 5** Detail of the welding nugget with martensitic structures and pores

according to Schaeffler [23]. The detail of the structure of the weld nugget also reveals the existence of micropores. These pores encapsulate leftover gases from CGS coating flaws and debris on the surfaces [22].

In Fig. 4, the Vickers hardness measurements are arranged in a 0.2×0.2-mm grid and were recorded with an automatic optical microscope that evaluates the diagonals of the indentations generated with a force of 2.942 N. The red lines in the interpolated area mark the borders between the steel plate, CGS layer, and aluminum, which is further divided into the as-cast state and the remelted area under the nugget. The microhardness mapping reveals the HAZ in the CGS layer, which is represented by the reduced hardness under and to the side of the nugget. The HAZ in the cold-gas-sprayed layer has a hardness of between 175 and 200 HV, marked with turquoise in Fig. 4, which is considerably lower than the compacted layer outside the bonding zone. Analogous to the difficulties of comparability between different CGS coating studies, as noted in Sect. 1, the comparability of the hardness values when heat treating the coating is only possible to a limited extent [12].

The weld nugget shows a maximum hardness of 416 HV due to the formation of martensitic structures [21]. 1.0991 forms a distinct heat-affected zone which can be visualized by etching. Depending on the temperature and cooling pace, the material generates martensitic and ferritic structures in this zone. This results in higher hardness in the HAZ of around 375 HV near the nugget, which reduces with increased distance.

The aluminum in the microsection shows the typical structure of mixed material resistance spot welds on materials with vastly different melting points, with the lower melting material forming a top-cap ellipsoidal remelted volume along the contact area [7, 24]. The melted area in the aluminum spans about the same size as the CGS-to-steel weld nugget, which can be traced back to the nugget being the main heat source [25], while the aluminum-to-CGS interface has no great influence on the heat generation and therefore on the nugget formation. Noticeable in the remelted area is the bloat of the aluminum in the direction of the weld nugget due to pores. These are formed by remelting high-pressure die cast aluminum and therefore releasing the trapped gas and vapors of the lubricants used in the casting process. In casting, the influence of the pores is reduced by pressurizing the liquid metal during solidification, thus compressing the gas pores [2]. The compressed gas pores and hydrogen pores are able to expand due to the reduced strength of the liquid aluminum.

In Fig. 6a, an overview of the pores in the remelted aluminum is displayed with both characteristic pore types in b and c. While the globular pores in the aluminum (Fig. 6b) can be traced back to trapped gas expanding metallurgically or to the casting process, the interdendritic elongated pores (represented in Fig. 6c) are solidification cavities. These are aided by the oxide layers as nucleation sites for micropores. The globular gas pores are formed in the completely liquid or early solidification phase, resulting in a round, smooth-walled appearance. The further the formation of dendrites has progressed, the more difficult it is for pores to form freely since they are impeded by the solidification of the dendrites, giving them a rough-walled appearance [2].

Due to the close-eutectic composition between aluminum and silicon, the aluminum alloy is expected to have a low tendency to crack and good casting properties, which exclude the presence of cracks due to mechanical stresses during the cooling process. The elongated micropores have a distinct dendritic wall structure, which is characterized by the round shape of the secondary dendrites, so the theory of hot crack formation can be rejected. The origin of the elongated micropores can be traced back to the hydrogen content

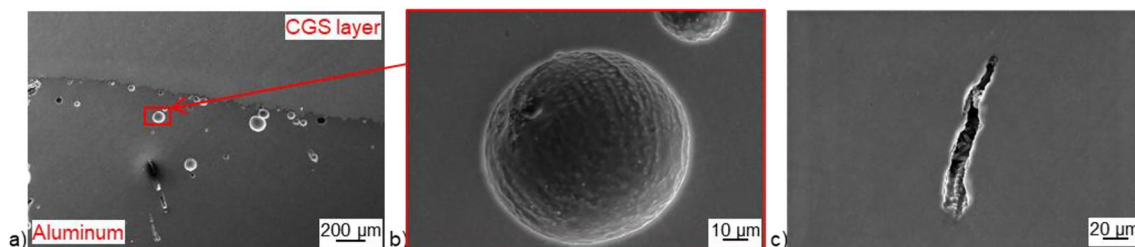


**Fig. 6** Types of pores inside the remelted aluminum: **a** globular metallurgical pores at the aluminum-to-CGS interface, **b** detailed section, and **c** elongated rough-walled pore

in the aluminum and its abrupt reduction of solubility in the solidification process. This leads to a supersaturation of hydrogen in aluminum, which further leads to the formation of pores during solidification. As a result, the pores nucleate late in the process, resulting in the creation of rough-walled and elongated dendrites between the existing dendrites [2].

The microstructure of the aluminum shows a directional structure formed by heat sources and sinks during solidification. These lines form due to local temperature reductions, resulting in the material's temperature falling below the liquidus temperature and promoting dendritic growth along the temperature gradient in the direction of the heat source [24, 25]. While welding, the temperature in the CGS-to-steel nugget formation phase exceeds the melting points of the steel partners, resulting in the superheating of the aluminum. In the cooling phase, the nugget solidifies first, heating the aluminum with its residual heat. Due to the high heat conduction of aluminum, the component cools the liquefied zone, resulting in horizontal solidification lines in the outer edge of the resolidified area of the aluminum (this effect is displayed in Fig. 7a). In this image, the HAZ at the outer edge of the resolidified area can be identified by the shift in the microstructure of the eutectic zones. The region is partially highlighted by red lines due to the slight microstructural variation between the cast and the structure of the heat-affected zone [26]. Later, a shift is noticeable, leading to a centering in the aluminum-to-CGS interface in the middle of the welding nugget. This indicates that the aluminum has a bigger impact on the cooling in the first stages than the electrodes. As mentioned before, the globular pores in the remelted aluminum deflect the solidification lines due to their early formation. In the hardness map, the remelted area can also be detected by an increased hardness of 110HV, which is marked by the red line in Fig. 4.

Contact between the liquid aluminum and the solid 316L CGS layer promotes the formation of Fe-Al-intermetallic phases, which can lead to brittle failure. In Fig. 7b, a fine layer (1) of IMP is noticeable in the aluminum-to-CGS interface. The thickness of the layer depends on the distance to the center of the spot weld and is accompanied by sharp branchlike marked with (2) structures near the center of the

weld. These branches are encapsulated in the remelted aluminum but also can be noted being exposed in pores near the aluminum-to-CGS interface in Fig. 7c. Small fragments of the intermetallic phases can be found near the pores indicating that these promote the nucleation of pores.

Macro- and microstructural, the most noticeable characteristic in resistance spot welding with a CGS inlayer is the reduction of defects in the HAZ due to the annealing of the coated inlayer. By relocating the trapped gases in the defects in a more energetic preferable state, globular pores are formed which can be noted in the HAZ as well in the nugget. Due to chemical composition and solidification rate of the nugget, a formation of martensitic structures is expected, which was confirmed by an analysis of the microstructure and the hardness.

The drastic difference in hardness between the as-sprayed state and the thermally modified state near the nugget, as well as the increase in hardness in the remelted aluminum, indicates the formation of a metallurgical notch. This statement was verified by testing the joint strength under shear load of the specimens welded for the study of the dynamic resistance with 600ms welding time. All welds in this preliminary test failed in the aluminum along the HAZ.

### 3.3 Microstructural investigation of the thermally affected cold-gas-sprayed coating

EBS and SEM are conducted to further evaluate the mechanisms occurring in the welding of cold-gas-sprayed materials. EBSD is used to visualize the strain indirectly in the quality map by illustrating the band contrast (BC) and gradients in lattice orientation in the grains. The band contrast analysis is used to display the signal quality detected by the EBSD detector, meaning the intensity of the Kikuchi bands. Lighter pixels represent a better agreement between the detected and calculated according to the expected bands and darker ones are of a worse agreement due to, for example, distortions of the lattice structure [27].

In Fig. 8, the BC of the EBSD mapping of a non-thermally stressed CGS layer is displayed. During cold gas spraying, the 316L particles experience high deformation

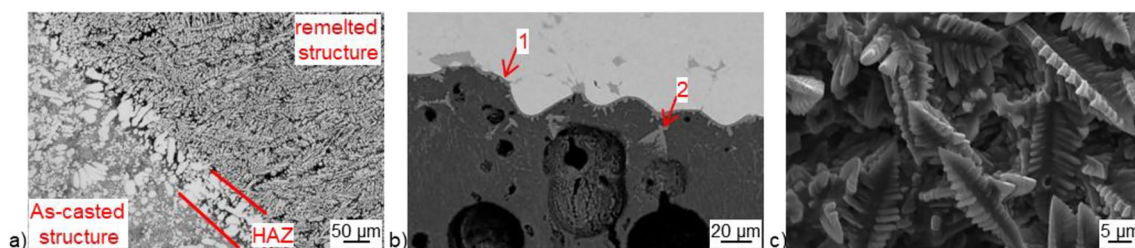


**Fig. 7** **a** Horizontal solidification lines in the edge of the remelted area. **b** Pores and IMP-layer and branchlike structures in a microsection. **c** Exposed branchlike IMP structures in a pore



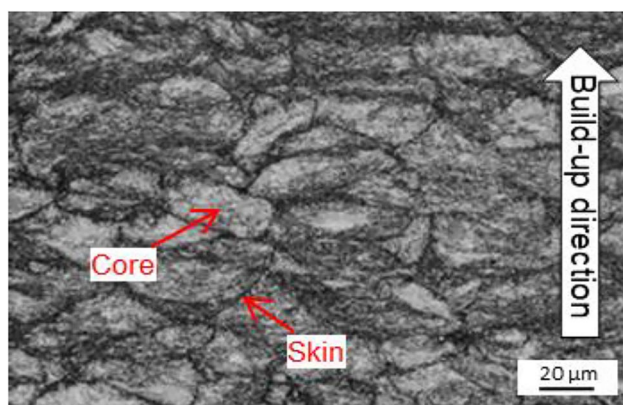


**Fig. 8** BC image of as-sprayed CGS inlayer with detectable particles

which results in a work-hardened state and in residual stresses [28]. The darker areas, and therefore the dislocations, are concentrated along the particle boundaries. Consequently, the state of deformation between the skin and the core of the particles is inhomogeneous [29].

An overview of the joint is presented in Fig. 9, which displays the welding nugget at the top, the aluminum substrate on the bottom, and the CGS layer in between an SE-image (a) and the corresponding EBSD image (b). In (a), the SE-image, a reduction of the defect density can be noted in the CGS layer near the nugget and intermetallic phases, as well as pores in the aluminum, which were already observed in the microscopy section of this paper. Figure 9b shows the inverse pole figure (IPF) map of the same section of the area of joint; the grains are displayed by their crystal orientation with the corresponding color map. The nugget shows a homogeneous grain size with some black areas further indicating martensitic phases, whose distortion results in a lower degree of detection, resulting in a black pixel analogous to the BC. In the aluminum substrate, large columnar grains can be visible, allowing the separation of grains.

The cold-gas-sprayed layer which is hardly detectable in its as-sprayed state (Fig. 8) can be mostly displayed in the EBSD analysis after the welding process. Although the

detectability and grain size are not consistent in the cold-gas-sprayed inlayer, adjacent to the nugget, large grains can be noted without areas of insufficient signal quality. However, near the aluminum substrate, the grain sizes are considerably smaller, and areas of bad signal quality marked by the black areas are noticeable.

The aluminum-to-CGS interface seems not to be fully relaxed and contains residual strain in the grains. This gradient of grain size and signal quality in the CGS layer between the nugget and the aluminum substrate indicates different thermal and mechanical conditions resulting in different annealing stages inside the coating. The degree of annealing depends on the previous dislocations in the material, the annealing temperature, and the time. The process can be divided into three phases: recovery (where residual dislocations in the lattice structure are reduced while grain deformation remains), recrystallization (where new grains generated are significantly smaller than the original grains), and grain growth (which results in a lower number of large equiaxial grains). The hardness reduces over the stages of the annealing with the largest reduction in the recrystallization phase [12].

Two bonding areas of the nugget-to-CGS interface are displayed in Fig. 10. The BC image presented in (a) is the bonding zone on the edge of the nugget to the CGS layer, while (b) and (c) display the area under the nugget with band contrast and the corresponding IPF color map. In the BC, the darker finer structure represents the nugget, showing the distorted lattice structures of the martensite. These structures are also visible in the IPF image in (c). The austenitic CGS layer in both (a) and (b) has a coarser and lighter structure, with large equiaxial grains visible at the bonding zone between the nugget and inlayer. Differences in maximal grain sizes between (a) and (b) are visible in the CGS layer, as is the reduction of grain sizes with increasing distance to the nugget.

The average size of the grains near the nugget-CGS bonding zone in (b) measures  $12.5\mu\text{m}$ , while  $25\mu\text{m}$  further away from the nugget, the average size reduces to  $7.1\mu\text{m}$ . In the first layer of grains in contact with the

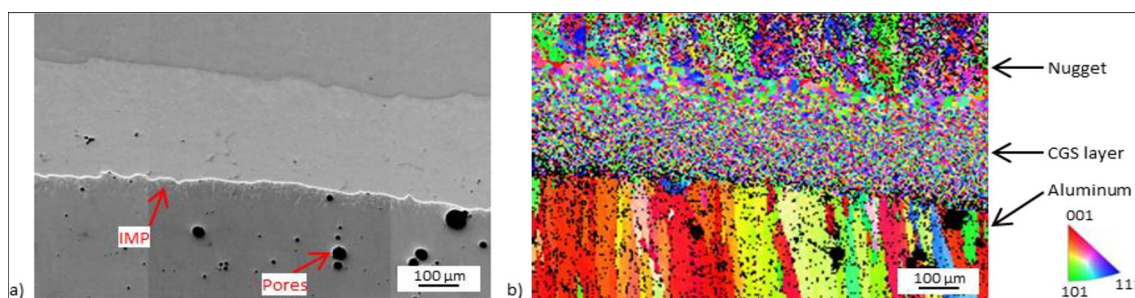
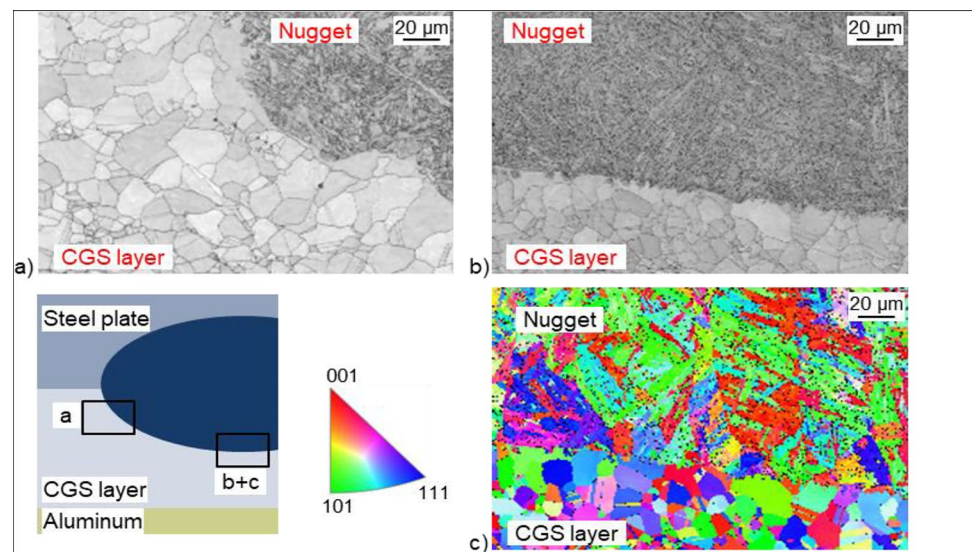


**Fig. 9** A SE-overview and the corresponding EBSD-IPF map of nugget. **b** CGS-layer and aluminum



**Fig. 10** Band contrast images of the cold-gas-sprayed inlayer and the nugget interface near the edge (a) and under the nugget (b). c The identical area as b in IPF color map



nugget, a lack of twins is noticeable in both (a) and (b), while the following grains mostly have twins. The lack of twins indicates the transgression of the recrystallization phase into the grain growth phase, in which the grain boundaries consume small grains and their twins without forming new twin boundaries [30, 31]. The main parameters for the formation of annealing twins are the prior deformation [32] and the annealing temperatures, as Sundararajan et al. noted [20]. Globular pores are visible at the grain boundaries which are formed during the recrystallization of the grains and consist of the gases entrapped in defects during the cold gas spraying process.

Due to the shorter distance between the nugget and the aluminum substrate in (b), a steeper temperature gradient is expected than in (a), which is located at the edge of the nugget, where the longer distance to the aluminum substrate results in a lower cooling rate. The different temperature gradients occurring can be noted in the grain growth as well as in the twinning density between the studied areas under and at the edge of the nugget, where in the latter these effects can be noted in a wider area.

The annealing stages differ regionally due to the uneven deformation between the particle's core and skin, as well as

the gradient of the thermal load. This is also reflected by the different size of the hardness reduction in Fig. 4.

### 3.4 Modification of the cold-gas-sprayed inlayer during welding near the aluminum substrate

Near the aluminum-to-CGS interface, lower temperatures are expected due to the higher thermal conductivity of the aluminum substrate. Figure 11a and b shows the identical section in BC and IPF of the aluminum-to-CGS interface, revealing smaller grains and distorted areas in the CGS layer as well as intermetallic phases in the aluminum.

The size of the grains near the aluminum (around  $2\mu\text{m}$ ) is considerably smaller compared to the grains near the nugget in Fig. 10, which have experienced grain growth. This observation, as well as large sections without distinctive grain borders like the ones marked by the dashed circle in Fig. 11b, indicates that the grains are not fully annealed and have not reached the recrystallized state.

The annealing of cold-gas-sprayed 316L is not yet studied enough for short temperature cycles as they occur during resistance spot welding. Brassart et al. [33] studied the influence of temperatures of 800 and  $1000^\circ\text{C}$  for 3 and 2 s,

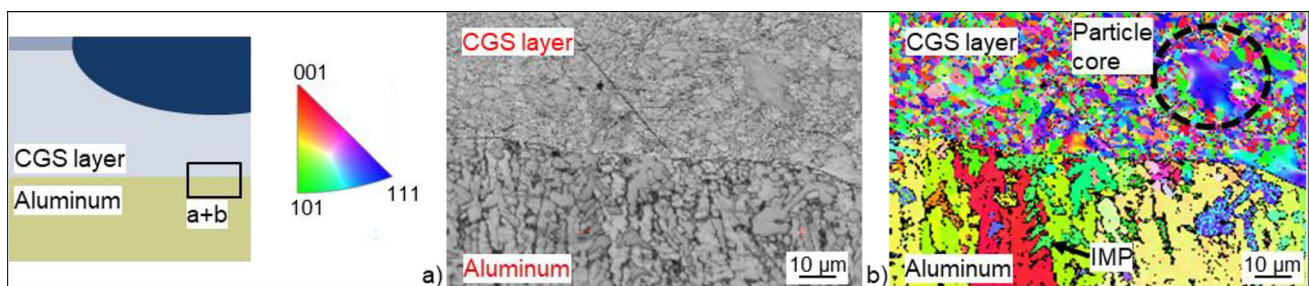


**Fig. 11** a Band contrast. b IPF image of the CGS layer near the aluminum in the middle of the nugget

respectively, which is about twice the welding time applied in this investigation. It is suggested that three states of recrystallization are recognizable, which are summarized in Table 2, along with their corresponding heat treatments. The 26 s above 1000 °C needed for a full recrystallization cannot be reached during the resistance spot welding process, but this experiment gives a brief idea of what grain structure can be expected with higher temperatures.

This lower grain size near the aluminum can be explained by lower temperatures and faster cooling conditions during and after welding, but also by fewer particle deformations near the softer substrate. As temperature, time, and degree of deformation are the main parameters in the recrystallization process, a fully recrystallized state of the particles near the aluminum substrate cannot be achieved. This effect is evident in the area marked with a black dotted circle in Fig. 11b. Partially recrystallized areas resulted from reduced deformation of the particle core in conjunction with lower temperatures. These areas show a gradient within their borders, which can lead to non-detectable areas at lower magnifications, as in Fig. 9b.

Near the aluminum, different effects are evident from the welding of the intermediate layer than in the vicinity of the welding zone. While large, recrystallized, and grown grains are formed in the latter, smaller grains can be seen near the substrate. The lesser particle deformation during coating, along with the lower temperature stress, results in isolated areas that are not entirely recrystallized.

## 4 Conclusion

Using a cold-gas-sprayed layer for aluminum-to-steel resistance spot welding enables a mixed material joint by separating the bonding interfaces between aluminum-to-inlayer and inlayer-to-steel. The inlayer is adhered to one side by mechanical joining and to the other side by a welding nugget. This allows the use of standardized steel-to-steel welding equipment for mixed material joints.

To assess its applicability in highly stressed applications, a study of the mechanical strength and failure of the joint is required. The interaction of the weld with the CGS coating must also be researched further in order to determine an optimum between the alteration of the inlayer during welding and the nugget size, as well as the effect of defect density and work-hardened and the recrystallization of the CGS layer and

mechanical performance of the joint due to the structural integrity of the coating.

The conclusions of the investigations are as follows:

- A temperature gradient develops during the welding process in which the nugget acts as a heat source and the aluminum substrate acts as a heat sink. This, in combination with the inhomogeneous deformation between the skin and cores of the particles during the coating process, leads to a gradient in the mechanical properties of the cold-gas-sprayed layer between the CGS-to-steel faying surface and the aluminum.
- Before the formation of the welding nugget in the faying surface between the cold-gas-sprayed inlayer and the steel plate can be noted in the resistance spot welding process, a reduction in defect density in the cold-gas-sprayed inlayer is visible. The defects reform into small globular cavities which can be found at the borders of the newly formed grains.
- During welding, the cold-gas-sprayed inlayer goes through different annealing stages, whereas the first layer of grains in contact with the nugget experiences grain growth, resulting in large grains as well as a regress of twins in the austenitic material of the inlayer. The grains near the aluminum do not exceed the recrystallization stages. The less deformed cores near the softer aluminum substrate sporadically remain in the as-sprayed state with residual stresses.
- The high-pressure die cast aluminum under the nugget will be liquefied mainly due to the heat conductivity from the CGS-to-steel weld. The entrapped gases in the aluminum, due to the high-pressure die casting process, lead to the formation of a bloat and pores under the welding nugget. The rapid solidification after the welding process due to the high thermal conductivity of the surrounding aluminum leads to an increased hardness in the remelted zone.
- The recrystallization process of the formerly work-hardened CGS inlayer results in a reduction of the hardness in the heat-affected zone, indicating a formation of a metallurgical notch. In preliminary testing, a failure along the HAZ was verified.

Resistance spot welding of high-pressure die cast aluminum to steel with a cold-gas-sprayed inlayer is an innovative connection technology for the transportation industry

**Table 2** States of recrystallization in cold-gas-sprayed coatings [25]

States	Core	Skin	Heat treatment
Recovered coating	Advanced recovery	Starting recrystallization	3 s at 800 °C
Partially recrystallized coating	Advanced recrystallization	Fully recrystallized	2 s at 1130 °C
Fully recrystallized coating	Fully recrystallized	Fully recrystallized	26 s at 1010 °C

that demonstrates benefits in terms of cycle time and production costs over current joining methods.

**Funding** Open Access funding enabled and organized by Projekt DEAL.

## Declarations

**Conflict of interest** The authors declare no competing interests.

**Open Access** This article is licensed under a Creative Commons Attribution 4.0 International License, which permits use, sharing, adaptation, distribution and reproduction in any medium or format, as long as you give appropriate credit to the original author(s) and the source, provide a link to the Creative Commons licence, and indicate if changes were made. The images or other third party material in this article are included in the article's Creative Commons licence, unless indicated otherwise in a credit line to the material. If material is not included in the article's Creative Commons licence and your intended use is not permitted by statutory regulation or exceeds the permitted use, you will need to obtain permission directly from the copyright holder. To view a copy of this licence, visit <http://creativecommons.org/licenses/by/4.0/>.

## References

- Li D, Chrysanthou A, Patel I et al (2017) Self-piercing riveting—a review. *Int J Adv Manuf Technol* 92:1777–1824. <https://doi.org/10.1007/s00170-017-0156-x>
- Ma Y, Yu W, Yuan Z et al. (2023) 3D characterization of pores expansion behavior in high pressure die castings during heat treatment. *Mater Charact* 197. <https://doi.org/10.1016/j.matchar.2023.112710>
- Kobayashi S, Yakou T (2002) Control of intermetallic compound layers at interface between steel and aluminum by diffusion-treatment. *Mater Sci Eng A* 338:44–53. [https://doi.org/10.1016/S0921-5093\(02\)00053-9](https://doi.org/10.1016/S0921-5093(02)00053-9)
- Winnicki M, Małachowska A, Korzeniowski M et al (2018) Aluminium to steel resistance spot welding with cold sprayed interlayer. *Surf Eng* 34:235–242. <https://doi.org/10.1080/02670844.2016.1271579>
- Arghavani MR, Movahedi M, Kokabi AH (2016) Role of zinc layer in resistance spot welding of aluminium to steel. *Mater Des* 102:106–114. <https://doi.org/10.1016/j.matdes.2016.04.033>
- Zhang F, Wang H-P, Hicks C et al (2013) Experimental study of initial strengths and hygrothermal degradation of adhesive joints between thin aluminum and steel substrates. *Int J Adhes Adhes* 43:14–25. <https://doi.org/10.1016/j.ijadhadh.2013.01.001>
- Sun X, Stephens E, Khaleel M et al (2004) Resistance spot welding of aluminum alloy to steel with transition material—from process to performance— Part I. *Exp Study Weld J* 83:188S-195S
- Huang R, Fukanuma H (2012) Study of the influence of particle velocity on adhesive strength of cold spray deposits. *J Therm Spray Technol* 21:541–549. <https://doi.org/10.1007/s11666-011-9707-0>
- Assadi H, Gärtner F, Stoltenhoff T et al (2003) Bonding mechanism in cold gas spraying. *Acta Mater* 51:4379–4394. [https://doi.org/10.1016/S1359-6454\(03\)00274-X](https://doi.org/10.1016/S1359-6454(03)00274-X)
- Oyinbo ST, Jen T-C (2019) A comparative review on cold gas dynamic spraying processes and technologies. *Manuf Rev* 6. <https://doi.org/10.1051/mfreview/2019023>
- Fardan A, Berndt CC, Ahmed R (2021) Numerical modelling of particle impact and residual stresses in cold sprayed coatings: a review. *Surf Coat Technol* 409. <https://doi.org/10.1016/j.surfcoat.2021.126835>
- Sova A, Grigoriev S, Okunkova A et al (2013) Cold spray deposition of 316L stainless steel coatings on aluminium surface with following laser post-treatment. *Surf Coat Technol* 235:283–289. <https://doi.org/10.1016/j.surfcoat.2013.07.052>
- Lindner T, Löbel M, Grimm M et al. (2022) Cold gas spraying of solution-hardened 316L grade stainless steel powder. *Metals* 12. <https://doi.org/10.3390/met12010030>
- Li W-Y, Liao H, Douchy G et al (2007) Optimal design of a cold spray nozzle by numerical analysis of particle velocity and experimental validation with 316L stainless steel powder. *Mater Des* 28:2129–2137. <https://doi.org/10.1016/j.matdes.2006.05.016>
- Oberdörfer Y, Chertov A, Maev RG (2019) Widerstandspunktschweißen von unterschiedlichen Metallen durch Verwendung einer Anpassschicht sowie dessen Prüfung mit Ultraschall in Echtzeit. DGZfP Jahrestagung 2019, May, Friedrichshafen, Germany. German <https://www.ndt.net/?id=24556>
- Borchers C, Schmidt T, Gärtner F et al (2008) High strain rate deformation microstructures of stainless steel 316L by cold spraying and explosive powder compaction. *Appl Phys A* 90:517–526. <https://doi.org/10.1007/s00339-007-4314-0>
- Zhou K, Cai L (2013) Online nugget diameter control system for resistance spot welding. *Int J Adv Manuf Technol* 68:2571–2588. <https://doi.org/10.1007/s00170-013-4886-0>
- Shinichiro A, Nobuhiro U (2017) Effect of cold-spray conditions using a nitrogen propellant gas on AISI 316L stainless steel-coating microstructures. *Coatings* 7. <https://doi.org/10.3390/coatings7070087>
- AL-Mangour B, Vo P, Mongrain R et al (2014) Effect of heat treatment on the microstructure and mechanical properties of stainless steel 316L coatings produced by cold spray for biomedical applications. *J Therm Spray Technol* 23:641–652. <https://doi.org/10.1007/s11666-013-0053-2>
- Sundararajan G, Sudharshan Phani P, Jyothirmayi A et al (2009) The influence of heat treatment on the microstructural, mechanical and corrosion behaviour of cold sprayed SS 316L coatings. *J Mater Sci* 44:2320–2326. <https://doi.org/10.1007/s10853-008-3200-2>
- Marashi P, Pouranvari M, Amirabdollahian S et al (2008) Microstructure and failure behavior of dissimilar resistance spot welds between low carbon galvanized and austenitic stainless steels. *Mater Sci Eng A* 480:175–180. <https://doi.org/10.1016/j.msea.2007.07.007>
- Alenius M, Pohjanne P, Somervuori M et al (2006) Exploring the mechanical properties of spot welded dissimilar joints for stainless and galvanized steels. *Weld J* 85:305S-313S
- Schaeffler AL (1949) Constitution diagram for stainless steel weld metal. *Met Prog* 56:680-680B
- Chen N, Wang H-P, Carlson BE et al (2017) Fracture mechanisms of Al/steel resistance spot welds in lap shear test. *J Mater Process Technol* 243:347–354. <https://doi.org/10.1016/j.jmatprotec.2016.12.015>
- Sun X, Khaleel MA (2004) Resistance spot welding of aluminum alloy to steel with transition material - Part II. Finite element analyses of nugget growth. *Weld J* 83:197S-202S
- Thijs L, Kempen K, Kruth J-P et al (2013) Fine-structured aluminium products with controllable texture by selective laser melting of pre-alloyed AlSi10Mg powder. *Acta Mater* 61:1809–1819. <https://doi.org/10.1016/j.actamat.2012.11.052>
- Yang L, Wang P, Luo X et al. (2021) Nanocrystallization of interfacial microstructure of deformed particles in cold sprayed Ti6Al4V deposits. *Mater Des* 210. <https://doi.org/10.1016/j.matdes.2021.110117>
- Suhonen T, Varis T, Dosta S et al (2013) Residual stress development in cold sprayed Al, Cu and Ti coatings. *Acta Mater* 61:6329–6337. <https://doi.org/10.1016/j.actamat.2013.06.033>

29. Zou Y, Qin W, Irissou E et al (2009) Dynamic recrystallization in the particle/particle interfacial region of cold-sprayed nickel coating: electron backscatter diffraction characterization. *Scr Mater* 61:899–902. <https://doi.org/10.1016/j.scriptamat.2009.07.020>
30. Jin Y, Lin B, Bernacki M et al (2014) Annealing twin development during recrystallization and grain growth in pure nickel. *Mater Sci Eng A* 597:295–303. <https://doi.org/10.1016/j.msea.2014.01.018>
31. Mahajan S (2013) Critique of mechanisms of formation of deformation, annealing and growth twins: face-centered cubic metals and alloys. *Scr Mater* 68:95–99. <https://doi.org/10.1016/j.scriptamat.2012.09.011>
32. Jin Y, Lin B, Rollett AD et al (2015) Thermo-mechanical factors influencing annealing twin development in nickel during recrystallization. *J Mater Sci* 50:5191–5203. <https://doi.org/10.1007/s10853-015-9067-0>
33. Brassart L-H, Besson J, Delloro F et al (2022) Effect of various heat treatments on the microstructure of 316L austenitic stainless steel coatings obtained by cold spray. *J Therm Spray Technol* 51:1725–1746. <https://doi.org/10.1007/s11666-022-01402-3>

**Publisher's note** Springer Nature remains neutral with regard to jurisdictional claims in published maps and institutional affiliations.